Technical Note: Range verification of pulsed proton beams from fixed-field alternating-gradient accelerator by means of time-of-flight measurement of ionoacoustic waves

Running title: Acoustic range verification of protons from FFA

Yuta Nakamura[1,†], Taisuke Takayanagi[2,3,†], Tomoki Uesaka[2], Mehmet Burcin Unlu[4], Yasutoshi Kuriyama[5], Yoshihiro Ishi[5], Tomonori Uesugi[5], Masanori Kobayashi[6], Nobuki Kudo[7], Sodai Tanaka[8], Kikuo Umegaki[8,9], Satoshi Tomioka[8], Taeko Matsuura[8,9,*]

[†] Yuta Nakamura and Taisuke Takayanagi contributed equally to this work.

***Corresponding author:** Dr Taeko Matsuura, Faculty of Engineering, Hokkaido University, North-15 West-7, Kita-ku, Sapporo, Hokkaido, 060-8638, Japan. Tel: +81-11-706-5254; Email: matsuura@med.hokudai.ac.jp

[1] Graduate School of Engineering, Hokkaido University, North-13 West-8, Kita-ku, Sapporo, Hokkaido, 060-8628, Japan

[2] Graduate School of Biomedical Science and Engineering, Hokkaido University, North-13 West-8, Kita-ku, Sapporo, Hokkaido, 060-8628, Japan

[3] Hitachi Ltd., 1-1 7-chome, Omika-cho, Hitachi-shi, Ibaraki, 319-1292, Japan

[4] Department of Physics, Bogazici University, Bebek, Istanbul, 34342, Turkey

[5] Institute for Integrated Radiation and Nuclear Science, Kyoto University, Osaka, 590-0494, Japan

[6] Planetary Exploration Research Institute, Chiba Institute of Technology, Chiba, 275-0016, Japan

[7] Faculty of Information Science and Technology, Hokkaido University, North-14, West-9, Kita-ku, Sapporo, Hokkaido, 060-0814, Japan

[8] Faculty of Engineering, Hokkaido University, North-13 West-8, Kita-ku, Sapporo, Hokkaido, 060-8628, Japan

[9] Proton Beam Therapy Center, Hokkaido University Hospital, North-15 West-7, Kita-ku, Sapporo, Hokkaido, 060-8638, Japan

Abstract

Purpose: Ionoacoustics is one of the promising approaches to verify the beam range in proton therapy. However, the weakness of the wave signal remains a main hindrance to its application in clinics. Here we studied the potential use of a fixed-field alternating-gradient accelerator (FFA), one of the accelerator candidates for future proton therapy. For such end, magnitude of the pressure wave and range accuracy achieved by the short-pulsed beam of FFA were assessed, using both simulation and experimental procedure.

Methods: A 100 MeV proton beam from the FFA was applied on a water phantom, through the acrylic wall. The beam range measured by the Bragg peak (BP)-ionization chamber (BPC) was 77.6 mm, while the maximum dose at BP was estimated to be 0.35 Gy/pulse. A hydrophone was placed 20 mm downstream of the BP, and signals were amplified and stored by a digital oscilloscope, averaged, and low-pass filtered. Time-of-flight (TOF) and two relative TOF values were analyzed in order to determine the beam range. Furthermore, an acoustic wave transport simulation was conducted to estimate the amplitude of the pressure waves.

Results: The range calculated when using two relative TOF was 78.16 ± 0.01 and 78.14 ± 0.01 mm, respectively, both values being coherent with the range measured by the BPC (the difference was 0.5−0.6 mm). In contrast, utilizing the direct TOF resulted in a range error of 1.8 mm. Five and fifty-fold averaging was required to suppress the range variation to below 1 mm for TOF and relative TOF measures, respectively. The simulation suggested the magnitude of pressure wave at the detector exceeded 7 Pascal.

Conclusion: A submillimeter range accuracy was attained with a pulsed beam of about 21 ns from an FFA, at a clinical energy using relative TOF. To precisely quantify the range with a single TOF measurement, subsequent improvement of the measuring system is required.

Keywords: proton therapy, range verification, ionoacoustics

1. Introduction

While proton therapy potentially allows better dose conformality compared to photon therapy because of the Bragg peak (BP), the full potential of the BP is yet to be exploited because of the range uncertainty.[1] Multiple sources of range uncertainty exist, including the conversion from the computed tomography (CT) value to stopping power ratio, anatomical changes of the patient, and organ motion, and much effort has been made to reduce this range uncertainty.[2] In vivo range verification during or shortly after treatment is a promising approach, and three methods have been proposed so far, namely prompt gamma detection (PGD),[3] positron emitter tomography (PET),[4] and ionoacoustics.[5] PGD and PET detect the gamma-ray arising from the nuclear reaction between protons and nuclei along the beam path. Both are currently used in clinics [6,7] and should detect the beam range in a few millimeter accuracy.[8]

The method using the ionoacoustic range verification is based on acoustic waves arising from a medium being hit by a pulsed proton/ion beam.[9] Unlike PGD and PET, requiring bulky and expensive gamma-ray detectors around patients, the acoustic wave detection system comprises a single or an array of hydrophones, requiring smaller space, and is more affordable.[10] Hayakawa et al.[11] first applied this method to a patient in which the feasibility of monitoring the proton dose distributions in patients was suggested by sensing acoustic pulses. Recently, many studies, both experimental and numerical, have been conducted to exploit the ionoacoustics to reduce the range uncertainty during proton therapy.[12] The experiments were performed using a linac,[13,14] a synchrotron,[11,15,16,17] a tandem accelerator,[18] a cyclotron,[19] a laser-plasma accelerator,[20] a hospital-based isochronous cyclotron,[21,22] and a synchrocyclotron,[23,24] all with positive results. Specifically, clinically relevant energy beams were used by Jones et al. (190 MeV and 230 MeV beams, accelerated by a clinical cyclotron)[21,22] and by Lehrack et al. and Patch et al. (energy between 145 MeV and 227 MeV, and energy ≥ 125 MeV, respectively, from a clinical synchrocyclotron). [23,24]

Although these results substantiate the usefulness of ionoacoustics, its clinical application has been hampered by the faint signal amplitude attainable hitherto. Pressure waves are generated efficiently in case thermal and stress confinement conditions are met, which is accomplished when pulse duration is no more than 5 μs[23] besides what signal amplitude is further increased if the pulse duration is shortened. Jones et al. modulated a clinical cyclotron ion source current to generate pulses of 17 μs, which are shorter than standard treatment delivery. However, in their work the wave amplitude obtained was limited to 25 mPa or below, at a maximum instantaneous beam current of 790 nA, with 11.5×10^7 protons, which entailed an averaging of 1024-fold.[22] Even with a superconducting synchrocyclotron, which achieved the shortest pulse among therapy machines (3.7 μs), Lehrack et al. reported that a dose of 10 Gy (2 pC per pulse ×1000 average) was required to reach submillimeter range accuracy.[23] Recently, with the same accelerator, Patch et al. demonstrated that the range verification is possible with the clinical dosage of 0.5 Gy, however, the customized fine-tuned detectors and amplifiers were required, which are not available commercially.[24] On the other hand, non-clinical machines such as tandem accelerator,[18] linac,[14] and laser-plasma accelerator[20] produce the shortest pulses of 8 ns, 250 ns, and 30 fs, respectively. In the last two instances, range measurement was done with a single[20] or 128-fold averaging,[14] conversely the beam energies with all accelerators being far below those that characterize therapeutic proton beams.

In the present study, we explored ionoacoustic range detection using a short-pulsed proton beam from an FFA.[25,26,27] The beam properties were within the range of that of clinical conditions [100 MeV, 1.12×10^8 proton/pulse (0.35 Gy at BP), lateral beam size ~ 5 mm], yet notably the pulse width was much smaller than that in clinical contexts ($\sigma \sim 21$ ns). Here we estimate the beam range by measuring the time-of-flight (TOF) of the direct wave emitted from the BP (referred to as γ-wave), as well as of the differences of TOF (referred to as relative TOF) between direct wave and the ones reflected at the phantom wall. Relative TOF was also used in prior studies[14,18,19] and has the considerable advantage of not being affected neither by the hydrophone positioning error nor the signal delay. The accuracy of the TOF methods was assessed in comparison with the range detected by the dose measurement by the BPC. Moreover, an acoustic wave transport simulation was performed to obtain the absolute amplitude of the pressure waves.

2. Materials and Methods

2.1 Proton beam from the FFA

The 100 MeV proton beam accelerated by the FFA at Kyoto University[28,29] was extracted at a repetition rate of 30 Hz and incident on the DigiPhant PT water phantom (IBA Dosimetry, Schwarzenbruck, Germany) through an acrylic wall of 1 cm. FFA designed for proton therapy could in principle accelerate protons up to 250 MeV[25] or 350 MeV[26] but only representative energy was used in this study. The pulse width was estimated at ~21 ns (1σ) according to the measurement using an EJ-200 plastic scintillator placed at the exit of the vacuum beam duct (Figure 1(B)). The scintillator coupled to a photomultiplier tube indirectly measures the beam pulse shape by detecting mainly the loss protons and gamma-ray emitted by nuclei activated by proton irradiation. The number of particles per pulse was measured using the Faraday cup and estimated as $(1.17 \pm 0.06) \times 10^8$, which is comparable to one pulse in a clinical setting.[30] The corresponding peak current was 0.4 mA.

2.2 Measurement of dose profiles

The Bragg curve shape was acquired by scanning the BPC (PTW34070, Freiburg, Germany) along the beam axis (Figure 2a). Beam range was defined at the BP maximum and estimated as R_{BPC} = 77.6 mm (mean of the two independent experiments). A transmission monitor Type 34014 (PTW, Freiburg, Germany) was used as the reference monitor. The lateral beam profile was obtained using a radiochromic film EBT3 attached to the surface of the water phantom (Figure 2b, c). The Satera MF8570Cdw (Canon Ltd.) was used as the film scanner, and at the surface of the water phantom, the respective beam size (1σ) was 4.7 mm, vertically, and 5.7 mm, horizontally.

2.3 Acoustic wave measurement

The unfocused type immersion hydrophone (V391-SU, Olympus, Waltham, USA) with a central frequency of 0.5 MHz was placed 20 mm downstream of the range measured by the BPC in the water phantom. The hydrophone was positioned by aligning the detector surface to the lasers mounted on the room walls. The sensitive volume is assumed to be located at the detector surface. The water employed was deionized and degassed, with its temperature maintained at 22°C throughout the experiment, corresponding to sound speed of 1488.4 m/s. As described later, the frequency spectrum of the acoustic waves originating from the BP has its maximum at around 100 kHz. On the other hand, the peak and upper/lower -6 dB frequencies of the hydrophone were 0.48, 0.63, and 0.33 MHz, respectively, according to the datasheet provided by the manufacturer. A control signal of the beam extraction kicker of the FFA was used for triggering data acquisition, and time zero was defined at the peak of the scintillator signal. Signals were amplified using a 46 dB amplifier (SA230-F5, NF Corporation, Japan), with a flat frequency response over the bandwidth of 1 kHz~100 MHz (+0.5, −3 dB), and then stored through digital oscilloscope at a 50 MS/s sampling rate, after averaging 5–50 events. A low-pass filter with a cutoff frequency of 1 MHz was used for filtering the RF noise at 8 MHz. We investigate whether the result depends on the incident beam energy by setting additional acrylic plates of various thicknesses (4 mm–20 mm) in front of the water phantom and repeated the measurement.

2.4 TOF and relative TOF metrics

In the previous research, beam range estimation has predominantly relied on the absolute TOF of the compression peak of the γ-wave. Here, beyond the conventional TOF of direct γ-waves (wavelet (a) in Figure 3), we explored the relative TOF metrics,[14,18,19] in order to avoid the bias of hydrophone positioning error (the difference between the TOF of wavelets (a) and (c) or (d) in Figure 3). Denoting the acoustic arrival time of each wavelet as $\tau^{(i)}$ ($i =$ a, c, d), the beam range (R) is estimated by

$$R = L_1 + L_2 + S_{\mathrm{acryl}} L_{\mathrm{wall}} - c_w\, \tau^{(a)},$$

when using the conventional TOF method, or by the expression

$$R = c_w \left(\frac{\tau^{(c)}-\tau^{(a)}}{2}\right) + S_{\mathrm{acryl}}L_{\mathrm{wall}} \text{ or } R = c_w \left\{\left(\frac{\tau^{(d)}-\tau^{(a)}}{2}\right) - \frac{L_{\mathrm{wall}}}{c_a}\right\} + S_{\mathrm{acryl}}L_{\mathrm{wall}},$$

if addressing relative TOF metrics. L_1, L_2, and L_{wall} are, respectively, the distances from the wall to the BP, and from the BP to the detector position, and the acrylic wall thickness. S_{acryl} represents the relative stopping power of acryl (= 1.16), while c_w and c_a are the sound speed in water and acryl, respectively.

2.5 Acoustic wave simulation

The waveform obtained from the experiment was further explored by conducting an acoustic wave simulation using a simple point-like detector with a constant frequency response and no delay. The thermoacoustic wave emission and transport equation, from the energy deposition of proton pulse, is described by the following expression,

$$\frac{1}{v^2}\frac{\partial^2 p}{\partial t^2} - \nabla^2 p = \left(\Gamma/v^2\right)E(\vec{r})I'(t),$$

where $E(\vec{r})$ corresponds to the distribution of transferred energy density [J/m^3]. $I'(t)$ is the time derivative of the normalized beam current [1/s], with the time integral of $I(t)$ over $-\infty < t < \infty$ having been normalized to 1, and Γ and v are the dimensionless Gruneisen coefficient and the sound velocity [m/s] of the medium, respectively.[31] In this simulation, we used the k-WAVE Matlab toolbox[32], which solves the coupled first-order differential equations for the acoustic particle velocity and density, rather than the above equivalent second-order equation. The acoustic properties of the water and acryl used as the simulation input was summarized in Table 1. Geant4 Monte Carlo code (ver.9.3)[33] was used to obtain $E(\vec{r})$, where the input beam parameters, including the mean energy of the incident protons, energy spread, and beam size were tuned to reproduce the measured Bragg curve and lateral beam profiles. For simplicity, protons were assumed to have momenta parallel to the beam axis at the phantom wall. The beam range, defined at the BP maximum, was R_{sim} = 76.3 mm, and the same number of protons per pulse and the detector position as the experiment were used in the simulation. The time-varying source was used in the k-WAVE simulation with the Gaussian pulse structure with a sufficiently small width (250 ns (1σ)). A perfectly matched layer is applied to the boundary, absorbing all outgoing acoustic waves and preventing reflection. The calculation was performed in 3D with a grid of $0.3 \times 0.3 \times 0.3$ mm^3. The time-step was set to 5 ns to ensure stability (Courant–Friedrichs–Lewy number < 1). Due to the limited computational memory capacity, the calculation volume was set as $50 \times 50 \times 100$ mm^3.

3. Results

3.1 Range estimation from measured acoustic waveform

Figure 4 shows the observed acoustic waveform without additional acrylic plates in front of the phantom, averaged over 50 measurements. The signal observed around time zero was the electromagnetic noise emitted from the beam extraction kicker of the FFA. As explained below, the hydrophone detected the four wavelets demonstrated in Figure 3.

Wavelet (a) shows the γ-wave from the BP. The arrival times of positive and negative peaks were 13.9 and 15.3 μs, denoted as $\tau_p^{(a)}$ and $\tau_n^{(a)}$, respectively. Because the pulse width of the FFA (FWHM of ~50 ns) is smaller than the size of BP divided by the sound speed (FWHM of 5.7 μs) by three orders of magnitude, the wavelet size (peak-to-peak distance of of 1.4 μs), is determined by the shape of the Bragg curve. The positive peak is higher than the negative peak, reflecting a higher dose gradient of the distal portion of the BP compared to the proximal portion.

Wavelet (c) and (d) are the γ-waves reflected at the water-acrylic wall and acrylic wall-air boundary, respectively. Taking into account the order of acoustic impedance (acryl > water > air) (Table 1), phase shift is 0° and 180° on reflection, respectively. As shown in the Appendix A, in theory, the reflected waves and direct wave are related by $p_{\text{reflected}}(t) \propto -\lambda\, p_{\text{direct}}(-t + \Delta t)$ where λ and Δt indicate the phase shift and the distance from the detector to its mirrored image reflected at the interface. The λ and Δt are +1 and $\frac{2(L_1+L_2)}{c_w}$ for wavelet (c) and -1 and $\frac{2(L_1+L_2)}{c_w} + \frac{2L_{\text{wall}}}{c_a}$ for wavelet (d), respectively. The negative peak, in the case of wavelet (c), arrived at 104.5 μs (denoted by $\tau_n^{(c)}$), and was superior to the positive one for the same reason specified above. Similarly, in the case of wavelet (d), the positive peak is higher than the negative peak and it arrives at 111.6 μs, symbolized by $\tau_p^{(d)}$.

Finally, wavelet (b) is the resonance wave generated in the acrylic wall. Because both water and air have a lower acoustic impedance than acryl, nodes occur at both ends. We did not use this wavelet for relative TOF, because the acoustic source of the resonance wave has a finite size and we did not have a clear idea which point in the wall can be regarded as the wave origin. Meanwhile, the resonance frequency was used to derive the sound speed of acryl in the experiment.

Figure 5A shows the frequency spectrum of the waveform in Figure 4. The sampled data over a time interval between 0 μs and 120 μs were Fourier transformed. The peaks at 0.12, 0.43, and 0.72 MHz originated from the resonance wave (b). The periodic dips on the spectrum are because of the repeated arrival of the γ-waves ((a), (c), and (d)).[34] To extract the spectrum of wavelet (a) (the time interval of $5\ \mu s \le t < 50\ \mu s$) and wavelets (c) and (d) ($100\ \mu s \le t < 120\ \mu s$), data out of these intervals were set to zero and zero-padding was applied until $t < 1{,}311\ \mu s$ before Fourier transformation (Figure 5B). The figure suggests that both frequencies of the direct and reflected γ-waves were concentrated below 0.6 MHz, with the maximum reached at ~60 kHz or ~340 kHz, respectively.

The upper row of Table 2 summarizes the relative TOF between (a) and (c) and between (a) and (d) and the estimated beam ranges. Negative peak maxima were selected for (a) and (c), whereas positive peak maximum was selected for (d), since, if the BP shape was symmetric along the beam line, such as Gaussian assumed in ref.[30], it should give the correct beam range. In addition, the smaller peaks of the reflected wavelets (positive peak in (c) and negative peak (d)) are challenging to address. Comparing these values with the range estimated by the BPC, the estimation error of two metrics $\tau_n^{(c)} - \tau_n^{(a)}$ and $\tau_p^{(d)} - \tau_n^{(a)}$ were both 0.6 mm. As a comparison, TOF and beam range calculated from the positive peak maximum of wavelet (a) were shown together, showing that the range error amounts to 1.8 mm with this metric.

Table 3 shows the water equivalent thickness (WEL) of the acrylic plates (actual thickness × 1.16) and the shift of the BP positions estimated from the change in the two metrics $\tau_n^{(c)} - \tau_n^{(a)}$ and $\tau_p^{(d)} - \tau_n^{(a)}$ from those without additional acrylic plates, respectively. The data show that the metrics can predict the BP position shift with a <0.2 mm accuracy.

3.2 Acoustic simulation

Finally, the red curves in Figure 4 represent the simulated acoustic waveform. The four wavelets observed in the experiment were observed in the simulation and the maximum pressure of about 7.5 Pa was reached. The lower row of Table 2 summarizes the TOF and range values calculated from the three metrics. Comparing these values with the range of the 100 MeV protons used as the input of the simulation (R_{sim} = 76.3 mm), the estimation errors of all metrics were within 1 mm.

The red curves in Figure 5 show the frequency spectrum of the wavelet (a) and wavelets (c) and (d) together. The spectrum shows that both the frequencies of the direct and reflected γ-waves were concentrated below 0.5 MHz, with the maximum reached at ~80 kHz or ~50 kHz, respectively.

4. Discussion

FFA is emerging as one of the accelerator candidates for upcoming proton therapy. This can achieve high beam intensities and stop acceleration when the required energy has been reached, permitting extraction at arbitrary energies. We have established that, with its short pulse duration, the ionoacoustic pressure amplitude reaches approximately 7.5 Pa at 2 cm distal to the BP, per 0.35 Gy dose at BP. In the meantime, the preceding research that exploited the proton energies greater than or equal to 50 MeV stated their pulse width as 2–17 μs, with the highest amplitude achieved per 2 Gy dose being 11 Pa, at 6.5 mm distal to the BP (Table 4).[19,22,23,35] This indicates that, at the same distance from the BP, the short pulse of FFA (20 ns) has the potential to yield a pressure of about 2−100 times that with the μs pulse, which gives an advantage to the FFA compared with other clinical machines (See the second right column in Table 4). Note that the large pressure generated by the cyclotron in ref[19] is partly due to the large Gy/pulse. If the

BP dose is normalized to 1 Gy, the pressure yielded by the FFA may be comparable to the synchrocyclotron, as shown in the rightmost column in Table 4.[23]

With the hydrophone used in this experiment, we could not validate the absolute pressure amplitude of the k-WAVE simulation since it does not have the pressure–voltage conversion constant. The k-WAVE simulation will have to be validated by a detector cross-calibrated with a reference transfer standard hydrophone in the future measurement. In a meantime, in a different experimental setting,[36] we showed that the k-WAVE simulation and the measured waveforms generated from FFA are similar but an absolute difference in the pressure amplitude was observed. The reduction of the difference between these waveforms may be possible by including detailed information about the structure and composition material of the hydrophone in the simulation, and thus further improvements in the accuracy of the simulation will be required.

In the current work, we applied the absolute and relative TOF metrics for range assessment, among which the former exploits the direct wave, and the signal amplitude is relatively larger than the reflection wave. Table 5 comprehends the maximum detected range variation amid 100 measurements and was given by several averages (each measurement consists of 1, 5, 10, and 50 events).[23] Regarding absolute TOF, the range variation was suppressed to 1 mm, even with a five-fold averaging. Nevertheless, it is subject to a detector-positioning error, as well as systematic errors prompted by the frequency-dependent delay of the hydrophone, which resulted in the range estimation error of 1.8 mm. Relative TOF is not impacted by these errors, and submillimeter range accuracy was achieved with this metric. However, since it uses the reflection wave, 50-fold averaging was required (Table 5). As Patch et al has denoted in their recent research, acoustic hardware fine-adjusted to the thermoacoustic emissions (around 100 kHz in case of the γ waves of this study) may be indispensable to achieve the range detection without averaging, and it is a subject we will address in further investigation.[24]

As in a preliminary study, we used a single element hydrophone, while Patch et al. explored a clinical transducer array to acquire a standard ultrasound image of the underlying anatomy, just before proton beam delivery. Their approach solves the above-stated issue of hydrophone positioning-derived error, by co-registering the BP and the underlying anatomy images. In addition, array transducers may be used to estimate the *in vivo* sound speed for the liver[37] and breast,[38] increasing the accuracy of *in vivo* range verification. Methods that utilize multiple hydrophones simultaneously to reconstruct the dose distribution were also explored in simulation study, using 3D filtered backprojection,[39] time-reversal algorithms,[40] and dictionary method.[41] Such lines of approach may be more suitable for heterogeneous tissues in clinical settings.

The simulation results with an ideal point detector shown in Table 2 indicate that the submillimeter range estimation error persists with the relative TOF metrics. The deviation of the range determined by $\tau_n^{(c)} - \tau_n^{(a)}$ or $\tau_p^{(d)} - \tau_n^{(a)}$ from the range used as the simulation input was 0.8 mm, reflecting the asymmetry of the Bragg curve along the beam path and is inherent to the beam shape. If the dissimilarity in the dose gradient of proximal and distal portions of the BP is minimized, which could be achieved by using the ripple filter to broaden the distal fall-off,[42] the accuracy of range estimation could be improved. On the other hand, the range error of 0.3 mm with the absolute TOF method could be due to definition of time zero and the acoustic wave arrival time. Even though this study made use of the compression peak of the γ-wave to characterize the arrival time of the direct γ-wave, as was done beforehand,[21,22,23] it does not necessarily lead to the correct TOF, as underlined by Jones et al.[22] and the analytical method.[43] Consequently, fine adjustment might be crucial to eliminate this systematic error.

5. Conclusion

The short-pulsed proton beams from FFA could generate large ionoacoustic waves at clinically relevant beam energy. Only five-fold averaging was required to suppress the range deviation to less than 1 mm for absolute TOF, yet the precision was restricted by systematic error arising from the detector positioning and signal delay. In contrast, the range determined using the relative TOF metrics was in agreement with the value calculated from the depth-dose measurement to better than 1 mm, but 50-fold averaging was essential, with the detection system employed in our work. This drawback may be untangled by resorting to fine-tuned detectors and amplifiers, which will be investigated in the future.

Acknowledgments

We wish to thank Dr. Hiroki Tanaka, Mr. Masayuki Fujii, Dr. Naoki Miyamoto, and Dr. Seishin Takao for their valuable support. This research was supported by JSPS KAKENHI Grant No. 21H02859 and JST FOREST Program (Grant Number JPMJFR200X, Japan)..

Competing Interests

We disclose conflict of interest as following; Authors Taisuke Takayanagi is paid from Hitachi, Ltd., Tokyo, Japan. Other authors have no conflict of interest.

Appendix A.

As described in the main text, the reflected γ-wave (wavelets (c) and (d) in Figures 4) is approximately obtained by applying time-reversal and sign inversion operations to the direct γ-wave (wavelet (a) in Figures 4) up to a scale factor. In this appendix, this relation is derived using a simplified model in which the BP is assumed as a one-dimensional finite length heat source lying on the z-axis (spreading over a range of $R_2 < z < R_1$, where $0 < R_2 < R_1$, as shown in Figure 6(a)).

As denoted in Sec. 2.5, the acoustic source term was expressed as $(\Gamma/v^2)E(\vec{r})I'(t)$. If the Gaussian pulse structure of the proton beam is assumed, $I'(t)$ is anti-symmetric under the time-reversal operation: $I'(t) = -I'(-t)$. In the following, the energy distribution of BP $E(\vec{r})$ is approximated as $E(z)\delta(x)\delta(y)$, where $\delta(x)$ is the Dirac delta function and $E(z)$ has finite support over $R_2 < z < R_1$. First, if we consider an infinite homogeneous water medium and solve the wave equation using the Green's function approach,[24] the pressure wave is expressed as

$$p(t,z) = \int_{-\infty}^{t} dt' \int_{R_2}^{R_1} dz'\, G(z,t;z',t') E(z') (\Gamma/v^2) I'(t') \tag{1}$$

where $G(z,t;z',t')$ is the Green's function satisfying the wave equation in three-dimensional free space

$$G(z,t;z',t') = \frac{\delta\left(t - t' - \frac{|z-z'|}{c_w}\right)}{4\pi|z-z'|}$$

and c_w is the sound speed in water. In the following, the detectors are assumed to be positioned at z_1 and z_2, satisfying $z_1 \gg \bar{R} + \Delta R$ and $z_2 \ll \bar{R} - \Delta R$, respectively, where $\bar{R} \equiv (R_1 + R_2)/2$ and $\Delta R \equiv R_1 - R_2$. Here, the denominator of the Green's function in the integrand could be approximated as $z_1 - \bar{R}$ and $|z_2 - \bar{R}|$, respectively, and Eq (1) reduces to

$$p_+(t, z_1) \sim \frac{1}{4\pi(z_1 - \bar{R})} \int_{R_2}^{R_1} dz'\, E(z') (\Gamma/v^2) I\left(t - \frac{z_1 - z'}{c_w}\right)$$

and

$$p_-(t, z_2) \sim \frac{1}{4\pi|z_2 - \bar{R}|} \int_{R_2}^{R_1} dz'\, E(z') (\Gamma/v^2) I\left(t - \frac{z' - z_2}{c_w}\right),$$

at z_1 and z_2, respectively. The subscript $\pm$ indicates the wave propagating toward the positive and negative *z* direction, respectively. By using $I'(t) = -I'(-t)$, we obtain the relation between $p_+(t, z_1)$ and $p_-(t, z_2)$ as

$$p_-(t, z_2) = -\xi\, \eta\, p_+(-t + \Delta t, z_1) \tag{2}$$

where ξ expresses the products of transmission (*T*) and reflection (*R*) coefficients at the interface of the heterogeneous media and is 1 in this case. $\eta = \frac{z_1 - \bar{R}}{|z_2 - \bar{R}|}$ is the geometrical factor and $\Delta t = \frac{z_1 - z_2}{c_w}$ is the acoustic wave propagation time between two detectors, indicating that with some simplifications, waves propagating in the positive and negative directions are related to the time-reversal and sign conversion up to a scale factor.

Next, we consider the geometry where the layers of air, acrylic wall, and water are stacked next to each other (Figure 6(b)). Here, Eq. (2) holds as follows. Because no phase change occurs at the acrylic wall-water boundary for wavelet (c), ξ is positive in Eq. (2), and ξ and Δt are $\xi = R_{\text{acryl−water}}$ and $\Delta t = \frac{2(L_1+L_2)}{c_w}$, respectively. However, for wavelet (d), the phase is shifted by 180° on reflection; hence, ξ becomes negative. In this case, ξ and Δt are $\xi = -\left(T_{\text{acryl−water}}\right)^2 R_{\text{acryl−air}}$ and $\Delta t = \frac{2(L_1+L_2)}{c_w} + \frac{2L_{\text{wall}}}{c_a}$, respectively.

Data availability

Data that support the findings of this study are available from the corresponding author upon reasonable request.

References

1. Paganetti H. Range uncertainties in proton therapy and the role of Monte Carlo simulations. Phys Med Biol. 2012;57(11):R99-R117.
2. Yang M, Zhu XR, Park PC et al. Comprehensive analysis of proton range uncertainties related to patient stopping-power-ratio estimation using the stoichiometric calibration. Phys Med Biol. 2012;57(13):4095-4115.
3. Krimmer J, Dauvergne D, Létang JM, Testa É. Prompt-gamma monitoring in hadron therapy: a review. Nucl Instrum Methods Phys Res A. 2018;878:58-73.
4. Knopf AC, Lomax A. In vivo proton range verification: a review. Phys Med Biol. 2013;58(15):R131-R160.
5. Hickling S, Xiang L, Jones KC, et al. Ionizing radiation-induced acoustics for radiotherapy and diagnostic radiology applications. Med Phys. 2018;45(7):e707-e721.
6. Richter C, Pausch G, Barczyk S, et al. First clinical application of a prompt gamma based in vivo proton range verification system. Radiother Oncol. 2016;118(2):232-237.

7. Nishio T, Miyatake A, Ogino T, Nakagawa K, Saijo N, Esumi H. The development and clinical use of a beam ON-LINE PET system mounted on a rotating gantry port in proton therapy. Int J Radiat Oncol Biol Phys Biology Physics 76.1. 2010;76(1):277-286.
8. Parodi K. Latest developments in-vivo imaging for proton therapy. Br J Rad. 2020;93(1107):20190787.
9. Kalinichenko A, Lazurik VT, Zalyubovsky II. Introduction to Radiation Acoustics. Boca Raton: CRC Press; 2002.
10. Assmann W, Parodi K. The Sound of ions: acoustic detection of high-energy beams. Nuclear Physics News. Nuclear Physics News. 2020;30(1):20-24.
11. Hayakawa Y, Tada J, Arai N et al. Acoustic pulse generated in a patient during treatment by pulsed proton radiation beam. Radiat Oncol Investig. 1995;3(1):42-45.
12. Parodi K, Assmann W. Ionoacoustics: A new direct method for range verification. Mod Phys Lett A. 2015;30(17).
13. Sulak L, Armstrong T, Baranger H et al. Experimental studies of the acoustic signature of proton beams traversing fluid media. Nucl Instrum Methods. 1979;161(2):203-217.
14. Patch SK, Santiago-Gonzalez D, Mustapha B. Thermoacoustic range verification in the presence of acoustic heterogeneity and soundspeed errors - Robustness relative to ultrasound image of underlying anatomy. Med Phys. 2019;46(1):318-327.
15. Hayakawa Y, Tada J, Inada T, Kitagawa T, Wagai T, Yosioka K. Acoustic pulse generation in excised muscle by pulsed proton beam irradiation and the possibility of clinical application to radiation therapy. J Acoust Soc Jpn (E). 1988;9(5):255-257.
16. Hayakawa Y, Tada J, Inada T, Wagai T, Yosioka K. Acoustic pulse generation in water by pulsed proton beam irradiation and its possible application to radiation therapy. Jpn J Appl Phys. 1989;28(S1):217-219.
17. Tada J, Hayakawa Y, Hosono K, Inada T. Time resolved properties of acoustic pulses generated in water and in soft tissue by pulsed proton beam irradiation—a possibility of doses distribution monitoring in proton radiation therapy. Med Phys. 1991;18(6):1100-1104.
18. Assmann W, Kellnberger S, Reinhardt S et al. Ionoacoustic characterization of the proton Bragg peak with submillimeter accuracy. Med Phys. 2015;42(2):567-574.

19. Patch SK, Kireeff Covo M, Jackson A, et al. Thermoacoustic range verification using a clinical ultrasound array provides perfectly co-registered overlay of the Bragg peak onto an ultrasound image. Phys Med Biol. 2016;61(15):5621-38.
20. Haffa D, Yang R, Bin J et al. I-BEAT: ultrasonic method for online measurement of the energy distribution of a single ion bunch. Sci Rep. 2019;9(1):6714.
21. Jones KC, Vander Stappen F, Bawiec CR et al. Experimental observation of acoustic emissions generated by a pulsed proton beam from a hospital-based clinical cyclotron. Med Phys. 2015;42(12):7090-7097.
22. Jones KC, Vander Stappen F, Sehgal CM, Avery S. Acoustic time-of-flight for proton range verification in water. Med Phys. 2016;43(9):5213-5224.
23. Lehrack S, Assmann W, Bertrand D et al. Submillimeter ionoacoustic range determination for protons in water at a clinical synchrocyclotron. Phys Med Biol. 2017;62(17):L20-L30.
24. Patch SK, Nguyen C, Dominguez-Ramirez D, et al. Thermoacoustic Range Verification During Pencil Beam Delivery of a Clinical Plan to an Abdominal Imaging Phantom. Radiother Oncol. 2021;S0167-8140(21):06164-8.
25. Keil, E., Sessler, A. M. & Trbojevic, D. Hadron cancer therapy complex using nonscaling fixed field alternating gradient accelerator and gantry design. Phys. Rev. ST Accel. Beams 10, 054701 (2007).
26. Garland JM, Appleby RB, Owen H, et al. Normal-conducting scaling fixed field alternating gradient accelerator for proton therapy. Phys. Rev. ST Accel. Beams. 2015;18(9), 094701.
27. Smith AR. Vision 20/20: proton therapy. Med Phys. 2009;36(2):556-68.
28. Ishi Y et al. Status report on FFAG accelerator complex at KURRI. Proc of the 12th Annual Meeting of Particle Accel. Soc. of Japan; vols 368-370; 2015.
29. Kuriyama Y et al. Status and development of a proton FFAG accelerator at KURRI for ADSR study. Proc Of 2011 Particle Accelerator Conference, THP027; 2011:2172-2174.
30. Ozoemelam I, van der Graaf E, van Goethem MJ, et al. Feasibility of quasi-prompt PET-based range verification in proton therapy. Phys Med Biol. 2020;65(24):245013.
31. Wang LV, Wu H-I. Biomedical Optics: Principles and Imaging. New York: Wiley; 2007.

32. Treeby, B. E. & Cox, B. T., Artn. k-Wave: MATLAB toolbox for the simulation and reconstruction of photoacoustic wave fields. J Biomed Opt. 2010;15:1117/1.3360308, DOI: doi PubMed: 02131410.
33. Allison J, Amako K, Apostolakis J et al. Recent developments in GEANT4. Nucl Instrum Methods A. 2016;835:186-225.
34. Kudo N, Zhang X, Yamamoto K. Measurement of the Wall thickness of the carotid artery using ultrasound radiofrequency Echo signals. J Med Ultrason. 1998;25(3):1-12.
35. Hayakawa used the short-pulsed proton beam (FWHM of 118 ns) from KEK synchrocyclotron and obtained 24 Pa per 1 Gy BP dose, but the position of the hydrophone was not available from the reference.
36. Takayanagi T, Uesaka T, Nakamura Y, et al. On-line range verification for proton beam therapy using spherical ionoacoustic waves with resonant frequency. Sci Rep. 2020; 10(1), 1-10.
37. Abe K, Arakawa M, Kanai H. Estimation method for sound velocity distribution for high-resolution ultrasonic tomographic imaging. J Med Ultrason. 2019;46(1):27-33.
38. Sanabria SJ, Ozkan E, Rominger M, et al. Spatial domain reconstruction for imaging speed-of-sound with pulse-echo ultrasound: simulation and in vivo study. Phys Med Biol. 2018;63(21):215015.
39. Alsanea F, Moskvin V, Stantz KM. Feasibility of RACT for 3D dose measurement and range verification in a water phantom. Med Phys. 2015;42(2):937-46.
40. Yu Y, Li Z, Zhang D, et al. Simulation studies of time reversal-based protoacoustic reconstruction for range and dose verification in proton therapy. Med Phys. 2019;46(8):3649-3662.
41. Freijo C, Herraiz JL, Sanchez-Parcerisa D, Udias JM. Dictionary-based protoacoustic dose map imaging for proton range verification. Photoacoustics. 2021;21:100240.
42. Matsuura T, Fujii Y, Takao S, et al. Development and evaluation of a short-range applicator for treating superficial moving tumors with respiratory-gated spot-scanning proton therapy using real-time image guidance. Phys Med Biol. 2016;61(4):1515-1531.
43. Kipergil EA, Erkol H, Kaya S, Gulsen G, Unlu MB. An analysis of beam parameters on proton-acoustic waves through an analytic approach. Phys Med Biol. 2017;62(12):4694-4710.

Figure captions

Figure 1. (A) Experimental setup. Proton beam accelerated by the FFA is incident on the water phantom, crossing the acrylic wall. A scintillator is set at the exit of the beam duct and it indirectly measures the beam pulse shape. A hydrophone is positioned 20 mm downstream of the beam range, facing this beam. (B) The signal measured by the scintillator and the Gaussian fitting curve.

Figure 2. (a) Bragg curve and (b, c) lateral beam profiles obtained by the Bragg peak ionization chamber and radiographic films, respectively. In (a), the solid curve shows the results obtained using Monte Carlo simulations.

Figure 3. Schematic representation of the wave propagation implied in TOF metrics to estimate the beam range. (a) Direct γ-wave from the BP, (c) the γ-wave reflected at the acrylic wall-water boundary, and (d) the γ-wave reflected at the boundary between the acrylic wall and the air. Because of the higher acoustic impedance of acryl compared to water and air, the resonance is formed in the acrylic wall. The resonance frequency of the wavelet (b), emitted from the wall, allowed to derive the sound speed in the acryl.

Figure 4. The time domain waveforms observed in the experiment (upper left) and the simulation (upper right), with the enlarged figures around wavelet (a) (lower left) and wavelets (c) and (d) (lower right). The red curves represent the simulation. In the lower figures, the simulation plot is shifted to match measured results for easing comparison. The thick arrows show the peaks selected for TOF or relative TOF metrics. The thin arrows refer to the peaks that were not used for TOF metrics.

Figure 5. Frequency spectrum of the waveforms shown in Figure 4, representing the experiment (black) and simulation (red). Frequency spectra of wavelet (a) (solid curves) and wavelets (c) and (d) (dashed curves) are shown in the right panel.

Figure 6. Schematic figure of the geometries considered in a simplified model in which the Bragg peak is assumed as a one-dimensional finite length heat source lying on the *z*-axis. (a) Homogeneous medium (b) Layer structure consisting of air, acrylic wall, and water

Tables

Table 1. Acoustic properties of water, acryl, and air.

	ρ(kg/m^3)	β(K^{-1})	v(m/s)	C_p(J/K/kg)	Γ	Z(Ns/m^3)
Water (22°C)	1000	2.06×10^{-4}	1488	4180	0.11	1.56×10^{6}
Acryl	1180	2.10×10^{-4}	2930	1400	1.29	3.46×10^{6}
Air	1.293	3.66×10^{-3}	340	1006	0.42	4.40×10^{2}

ρ: mass density, β: coefficient of volumetric thermal expansion, v: speed of sound, C_p: heat capacity at constant pressure, Γ: Gruneisen coefficient, and Z: acoustic impedance.

Table 2. Relative and absolute TOF of the wavelets (c) and (d) and of the wavelet (a), respectively, and the beam range estimated with these distinct metrics, both from the experiment (upper row) and simulation (lower row). The values are the mean and SE of 100 independent measurements (each consisting of 50 events).

		$\tau_n^{(c)} - \tau_n^{(a)}$	$\tau_p^{(d)} - \tau_n^{(a)}$	$\tau_p^{(a)}$
Experiment	Time (μs)	89.47 ± 0.02	96.27±0.01	13.98 ± 0.01
R_{BPC} = 77.6 mm	Range (mm)	78.16 ± 0.01	78.15 ± 0.01	75.80 ± 0.01
Simulation	Time (μs)	85.98	92.74	13.42
R_{sim} = 76.3 mm	Range (mm)	75.57	75.52	76.63

Table 3. The water equivalent thickness of the additional acrylic plates (actual thickness × 1.16) and the shift in the BP positions (mean ± SE), estimated from the variation in the two metrics $\tau_n^{(c)} - \tau_n^{(a)}$ and $\tau_p^{(d)} - \tau_n^{(a)}$ from those obtained without the acrylic plates.

Thickness of additional acrylic plates (mmWEL)	$\Delta\,(\tau_n^{(c)} - \tau_n^{(a)})$ (mmWEL)	$\Delta\,(\tau_p^{(d)} - \tau_n^{(a)})$ (mmWEL)
4.6	4.8 ± 0.03	4.6 ± 0.03
9.3	9.2 ± 0.03	9.5 ± 0.03
13.9	14.1 ± 0.04	14.1 ± 0.03
18.6	18.6 ± 0.04	18.5 ± 0.02
23.2	23.3 ± 0.04	23.3 ± 0.03

Table 4. List of the absolute pressure values in ionoacoustics that can be retrieved from previous research.

	Energy [MeV]	Pulse duration (FWHM) [μs]	Gy/pulse	Pressure, detector position (distance from the BP)	Expected pressure at 5 cm from the BP	Expected pressure per 1 Gy at 5 cm from the BP
cyclotron[22]	190	15-19	0.034	5.2 mPa[*a], 5 cm	29 mPa	0.85 Pa
synchrocyclotron[23]	145–227	2.5-3.7	0.01	58 mPa[*b], 5–10 cm	58–116 mPa[*c]	5.8–11.6 Pa[*c]
cyclotron[19]	50	1.76	2	11 Pa, 6.5 mm	1.4 Pa[*c]	0.72 Pa[*c]
FFA	100	0.047	0.35	7.5 Pa, 2 cm	3 Pa[*c]	8.6 Pa[*c]

[*a] This value is per 6.1 mGy according to the ref.[21] [*b] The maximum pressure amplitude of about 23 mV (Fig. 1 in ref.[23]) was converted to the pressure using the detector sensitivity (−168 (dB, re 1 V μPa^{-1})) and the amplifiers (40 dB). [*c]These values were roughly estimated assuming that the pressure size is inversely proportional to the distance from the BP. [22]

Table 5. The maximum variation of the detected range (in mm) among 100 measurements, with numerous measurement averages.

Number of averages	Total dose [Gy]	Time used for range detection		
		$\tau_n^{(c)} - \tau_n^{(a)}$	$\tau_p^{(d)} - \tau_n^{(a)}$	$\tau_p^{(a)}$
1	0.35	10.8	13.3	2.1
5	1.75	4.8	1.1	0.7
10	3.5	3.1	0.7	0.6
50	17.5	0.7	0.5	0.4

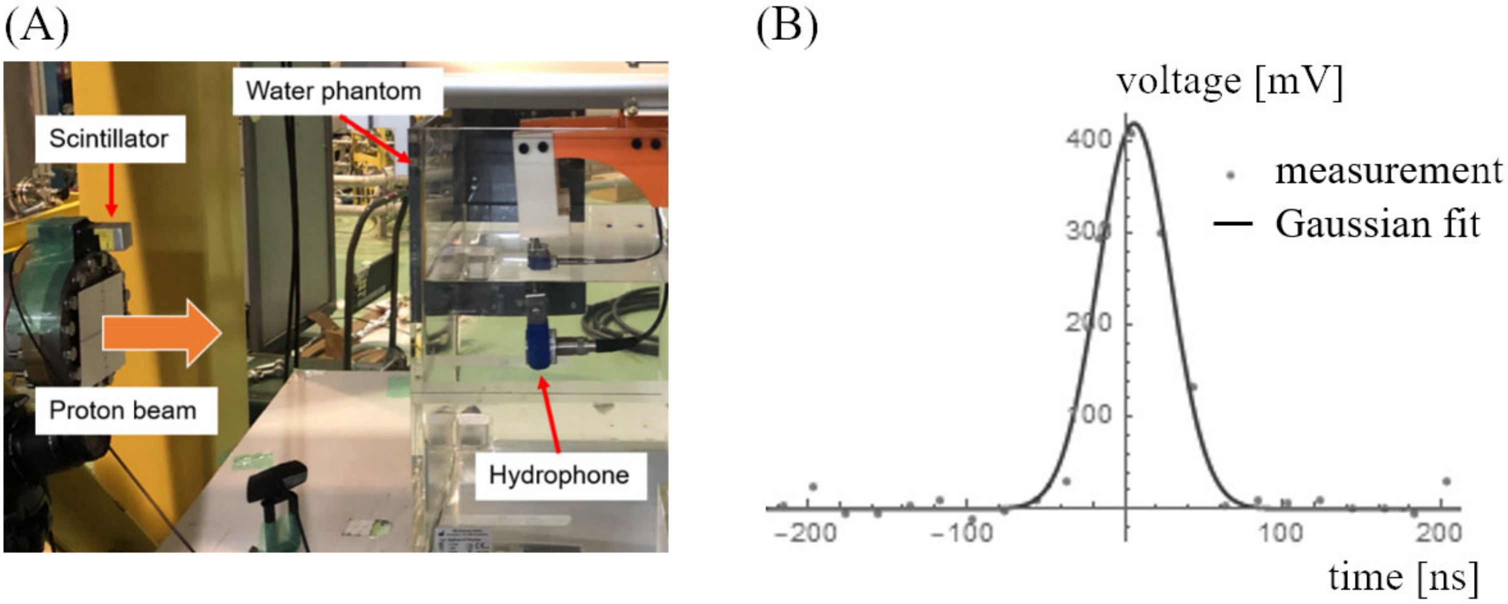
(A)
Water phantom
Scintillator
Proton beam
Hydrophone
(B)
voltage [mV]
400
300
200
100
measurement
Gaussian fit
-200
-100
100
200
time [ns]

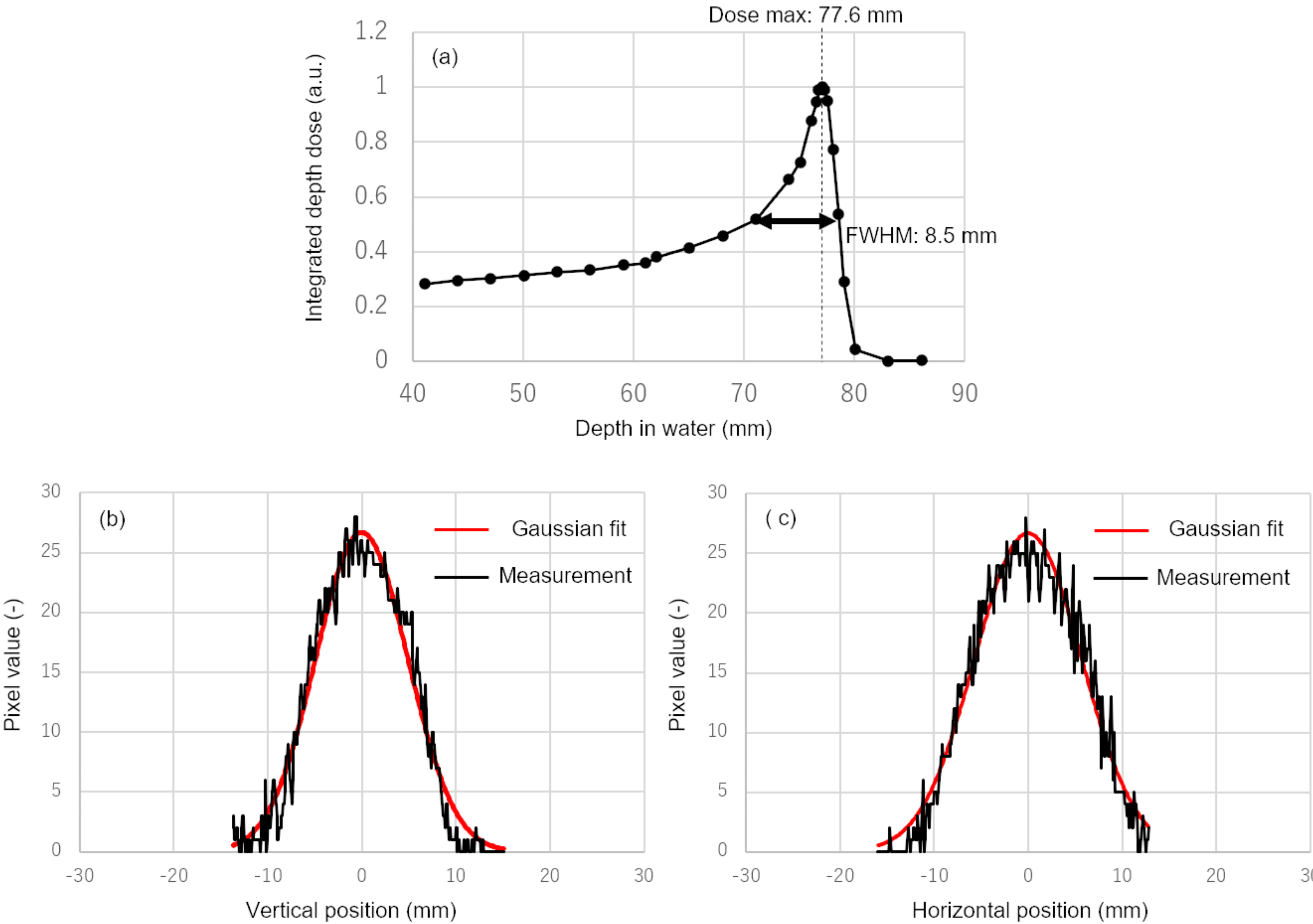
Dose max: 77.6 mm
(a)
FWHM: 8.5 mm
Integrated depth dose (a.u.)
1.2
1
0.8
0.6
0.4
0.2
0
40
50
60
70
80
90
Depth in water (mm)
(b)
Gaussian fit
Measurement
Pixel value (-)
30
25
20
15
10
5
0
-30
-20
-10
0
10
20
30
Vertical position (mm)
(c)
Gaussian fit
Measurement
Pixel value (-)
Horizontal position (mm)

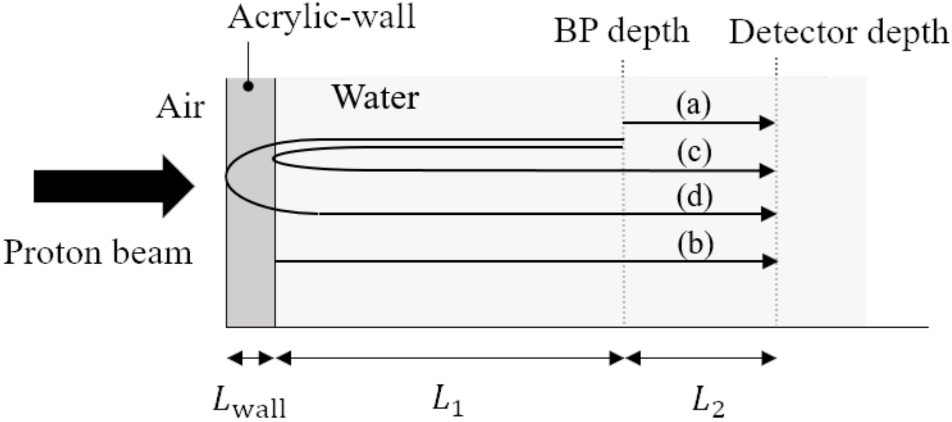
Acrylic-wall
BP depth
Detector depth
Air
Water
(a)
(c)
(d)
(b)
Proton beam
L_{wall}
L_1
L_2

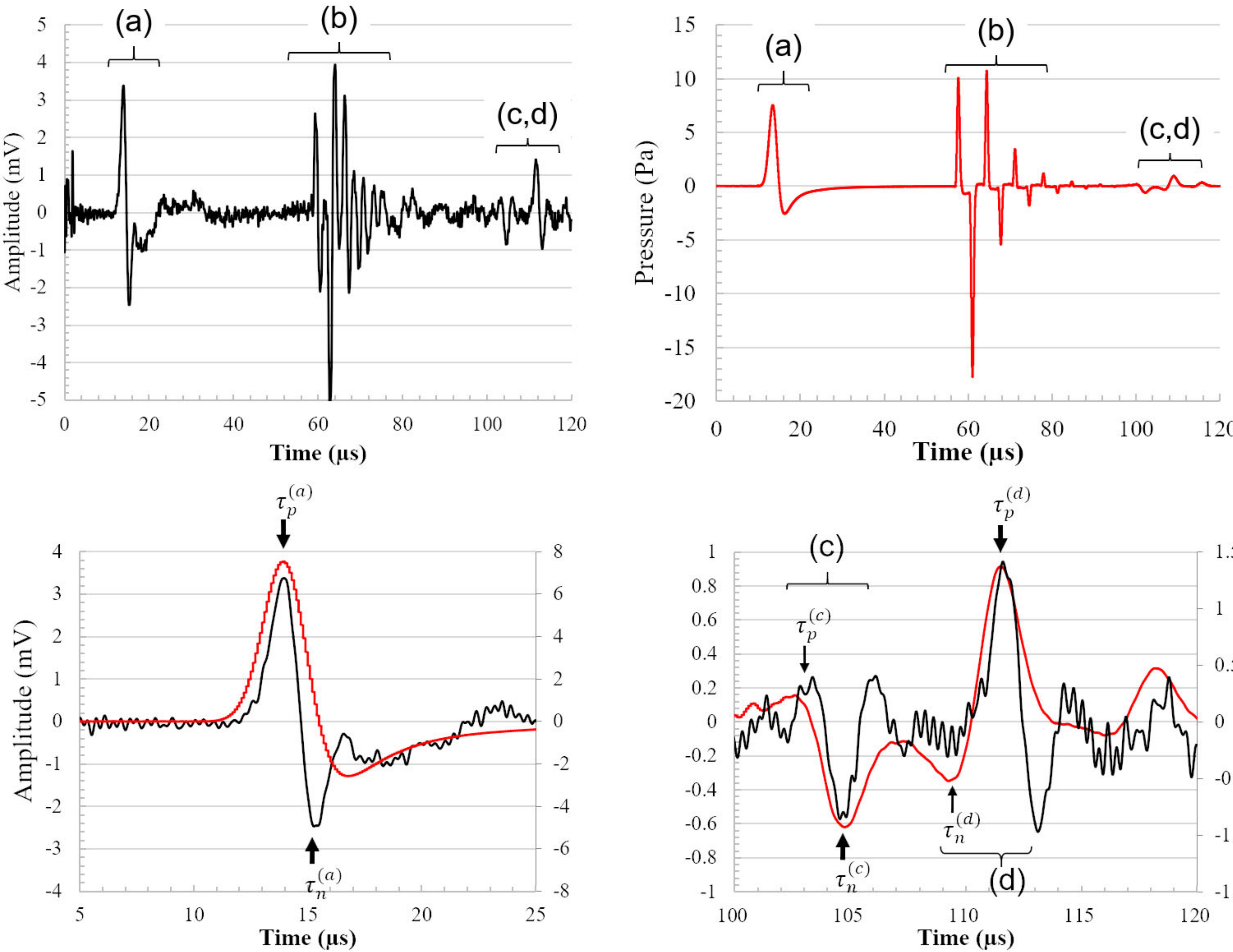

(a)
(b)
(c,d)
Amplitude (mV)
Time (µs)
Pressure (Pa)
$\tau_p^{(a)}$
$\tau_n^{(a)}$
(c)
(d)
$\tau_p^{(c)}$
$\tau_n^{(c)}$
$\tau_p^{(d)}$
$\tau_n^{(d)}$

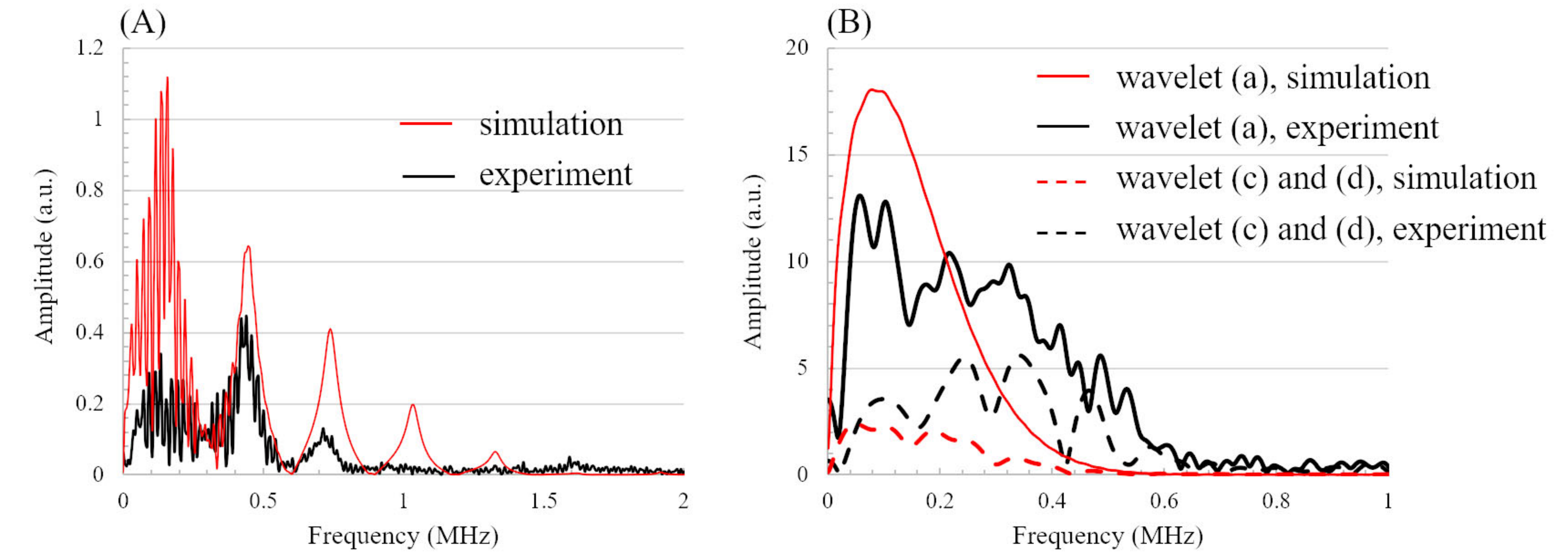
(A)
1.2
1
0.8
0.6
0.4
0.2
0
Amplitude (a.u.)
simulation
experiment
0
0.5
1
1.5
2
Frequency (MHz)
(B)
20
15
10
5
0
Amplitude (a.u.)
wavelet (a), simulation
wavelet (a), experiment
wavelet (c) and (d), simulation
wavelet (c) and (d), experiment
0
0.2
0.4
0.6
0.8
1
Frequency (MHz)

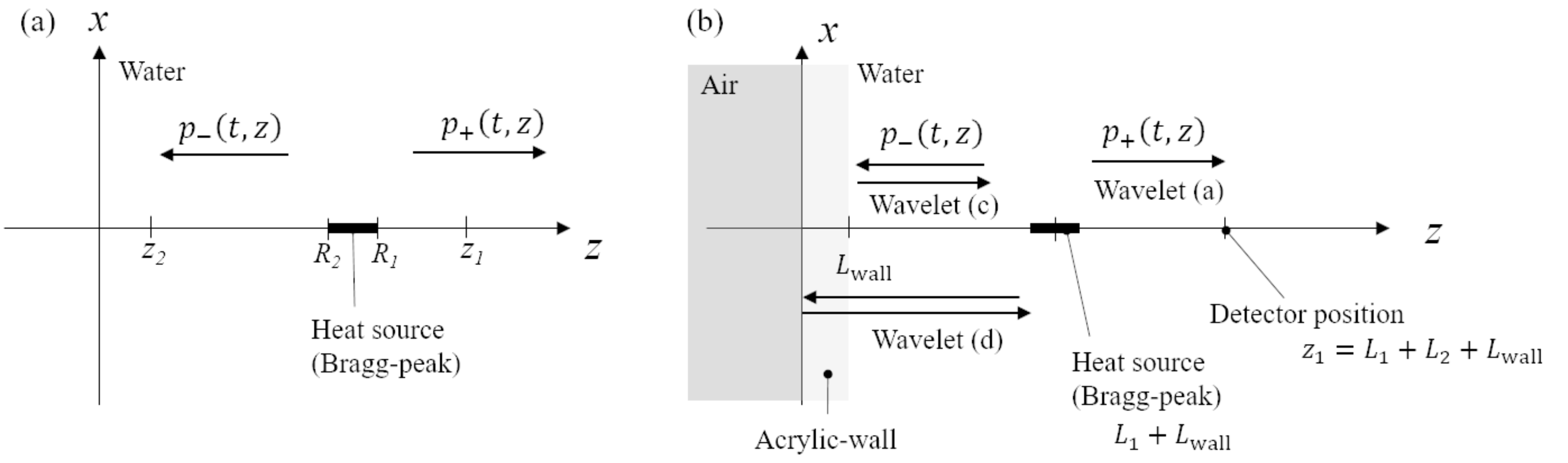
(a)
x
Water
$p_-(t,z)$
$p_+(t,z)$
z_2
R_2
R_1
z_1
z
Heat source
(Bragg-peak)
(b)
x
Air
Water
$p_-(t,z)$
$p_+(t,z)$
Wavelet (c)
Wavelet (a)
z
L_{wall}
Wavelet (d)
Detector position
$z_1 = L_1 + L_2 + L_{\mathrm{wall}}$
Heat source
(Bragg-peak)
$L_1 + L_{\mathrm{wall}}$
Acrylic-wall